Electrochimica Acta 401 (2022) 139484

Contents lists available at ScienceDirect

Electrochimica Acta

journal homepage: www.elsevier.com/locate/electacta

Investigating dopants to improve sintered $LiMn_2O_4$ spinel electrode electrochemical cycling limitations

Chen Cai[a], Gary M. Koenig Jr.[a,*]

[a] Department of Chemical Engineering, University of Virginia, 102 Engineers Way, Charlottesville, 22904-4741, VA, USA

ARTICLE INFO

Article history:
Received 20 August 2021
Revised 15 October 2021
Accepted 23 October 2021
Available online 30 October 2021

Keywords:
Lithium-ion battery
Sintered electrode
Doping
Electronic conductivity

ABSTRACT

Lithium-ion batteries have become prevalent for portable energy storage. Towards continuing to increase the energy density of batteries, engineering the electrode structure can provide improvements with regards to energy and power density. Sintered electrodes, which have no inactive additives, can achieve high areal loadings of over 150 mg electroactive material cm^{-2}, however, they have electronic and/or ionic transport resistance limitations as the electrode loadings and thicknesses increase. Herein, $LiMn_2O_4$ was investigated as a sintered electrode cathode material. $LiMn_2O_4$ is attractive as a relatively low cost and Co-free cathode option, but its relatively low electronic conductivity and fading due to Jahn-Teller distortion and/or manganese dissolution pose challenges that are exacerbated in sintered electrodes relative to composites. Thus the incorporation of dopants $LiMn_{2-x}M_xO_4$, where M = Cu or Al (in isolation or combination) and x ranged from 0 to 0.15, were investigated to understand how modifications to the material electronic conductivity and structural stability would impact sintered electrodes comprised of these materials. Improvement in sintered electrode electrochemical outcomes was observed for incorporation of both dopants.

1. Introduction

One route to increase the energy density in lithium-ion (Li-ion) batteries at the cell level is to increase the electrode thickness, because thicker electrodes result in greater relative fractions of the cell being electroactive material which stores/delivers energy [1,2]. However, as electrodes are made thicker, one challenging limitation is that ionic transport pathways become much longer resulting in substantial polarization and reduced rate capability due to depletion of ions in the electrode microstructure during charge/discharge [1]. Transport restrictions are exacerbated in thick composite electrodes which have conductive carbon and polymer binder additives, because these inactive species occupy the interstitial regions along with the electrolyte and make the ion pathways more tortuous. For example, relative to ideal hard sphere packing, the increase in the exponent associated with tortuosity (e.g., Bruggeman exponent) for composite electrodes with inactive additives has been reported to be over a factor of 3 [3,4]. To reduce the tortuosity associated with the inactive compounds, routes have been explored to process electrodes free of these additives [5–7]. One such system is "sintered electrodes", where solid electroactive Li-ion battery particles have been pressed together (e.g., via hydraulic compression) and undergo heat treatment resulting in a porous ceramic structure [8–14]. Compared to conventional composite electrodes, sintered electrodes typically have relatively high thicknesses (> 500 μm), resulting in high areal loadings of active material exceeding ~200 mg cm^{-2} [12]. Such electrodes reduce inactive mass dedicated to the electrode architecture, alleviate the additional ion transport restrictions associated with these additives, and with increased thickness decreases the relative allocation of other cell components such as separators and current collectors [2,8,9,11].

One important consideration with sintered electrodes is that they do not contain the conductive additives that facilitate electron transport through the electrode matrix in composite electrodes. With the absence of conductive additives, electrons must traverse to/from the current collector through the entire electrode thickness via conduction through the electroactive material itself. Materials such as $LiCoO_2$ (LCO) are well suited as a cathode material for sintered electrodes because the electronic conductivity is relatively high across a wide range of degrees of lithiation (over 95% of the lithiation range typically accessed in LCO has electronic conductivity over 10^{-1} S cm^{-1}) [11,15,16]. However, due to environmental [17] and cost [18] challenges, consideration of alternative cathode materials should be explored for sintered electrodes. One possibility, considered in this report, is the spinel-phase commercial Li-ion

* Corresponding author.
E-mail addresses: gary.koenig@virginia.edu, gmk3k@virginia.edu (G.M. Koenig Jr.).

https://doi.org/10.1016/j.electacta.2021.139484
0013-4686/

cathode material $LiMn_2O_4$ (LMO). LMO has potential advantages of earth-abundant transition metals, relatively low reported toxicity, and much lower cost than alternatives such as LCO [19–21]. However, the electronic conductivity of LMO (10^{-4}–10^{-5} S cm^{-1}) [22–25] is much lower than that of LCO, about 4 orders of magnitude [11,15,16]. This low conductivity presents a challenge in its use as a sintered Li-ion cathode material without restricting the operating rate/current density, unless the material can be modified to improve the electronic conductivity [26–30].

One route previously reported to modify LMO materials for Li-ion cathodes, targeted towards conventional composite electrodes, is to dope the LMO structure with other metals [31–37]. Doping has been pursued both to stabilize the LMO structure during cycling and towards attempting to improve the material electronic conductivity [31,38–43]. Guided by previous studies of LMO doping, herein the impacts of doping were investigated on the electrochemical properties of LMO sintered electrodes. While there already exists a literature on doping of LMO and the impacts on electronic conductivity, structural stability, and electrochemical cycling, the novelty in this manuscript is in applying these doping material concepts to sintered electrodes. The lack of conductive additives and the reliance on particle-particle contacts in sintered electrodes means they are even more dependent on the electroactive material to be structurally resilient and electronically conductive. Thus, it was expected that sintered electrodes would especially benefit from dopants that improved on the relatively low conductivity of LMO material. In particular, the dopants Al and Cu into the LMO were explored to understand the impact on the electrochemical properties of the final sintered electrodes.

2. Methods and materials

2.1. Pristine and doped $LiMn_2O_4$ synthesis

To synthesize $LiMn_2O_4$ (LMO) first an Mn oxalate precursor was prepared. 100 mM of sodium oxalate ($Na_2C_2O_4$, Fisher Chemical) and 10 mM of sodium citrate dihydrate ($Na_3C_6O_7H_5{\cdot}2H_2O$, Sigma-Aldrich) were dissolved into 400 mL of deionized (DI) water in a 1000 mL beaker, and separately 100 mM of manganese sulfate monohydrate ($MnSO_4{\cdot}H_2O$, Fisher Chemical) was dissolved in 400 mL of DI water in another 1000 mL beaker. Both solutions were preheated to 60 ºC before adding the manganese sulfate solution into the oxalate/citrate solution all at once. The precipitation reaction was kept at 60 ºC using a stirred hot plate at 300 RPM, and the reaction proceeded for 30 min. After the 30 mins of reaction, the precipitate was collected by via vacuum filtration, rinsed with 1.6 L of DI water, and dried at 80 ºC overnight in an air atmosphere. The resulting precipitate was $MnC_2O_4{\cdot}2H_2O$, as has been previously reported using similar methods [44,45].

To convert the precursor to electroactive LMO-type battery material, the $MnC_2O_4{\cdot}2H_2O$ was blended with Li_2CO_3 (Fisher Chemical) for a target molar ratio of 1.05:2 Li:Mn. For cases where the LMO was doped with Cu or Al, in addition to Li_2CO_3 the oxalate precursor was also blended with CuO (Alfa Aesar, for Cu doping) or Al_2O_3 (Alfa Aesar, for Al doping) for a target molar ratio 1.05:2-x:x, where $x = 0$, 0.05, 0.1, and 0.15 (dopant level) and the molar ratios represent Li:Mn:Cu or Li:Mn:Al (depending on whether Cu or Al substitution for Mn was targeted). Mortar and pestle were used to mix the powders by hand for 10 min before transfer into a furnace (Carbolite CWF 1300). The temperature profile used for calcination was to heat to 900 ºC via ramping up the temperature at 1 ºC min^{-1}, holding the temperature at 900 ºC for 6 h, ramping the temperature down at 1 ºC min^{-1} to 700 ºC, holding at 700 ºC for 10 h, and then ramping the temperature down to 30 ºC at a rate of 1 ºC min^{-1}. The furnace atmosphere was air. The materials extracted from the furnace were the final electroactive material powders.

2.2. Electrochemical evaluation

For composite electrode cells, cathodes were processed by mixing the electroactive material powder with acetylene carbon black (CB, Alfa Aesar), and polyvinyl pyrrolidone (PVP, Sigma Aldrich, 360 kDa molecular weight) using ethanol (Fisher) as solvent with a mass ratio of 8:1:1 active material:CB:PVP. Mixing was performed in a slurry mixer (Thinky AR-100) at 2000 RPM for 4 min followed by sonication for 5 min and then another 4 min at 2000 RPM in the slurry mixer. The slurry was casted onto an aluminum foil using a doctor blade with a 400 µm gap height. The loadings for all experiments ranged from 4.4 – 9.1 mg electroactive material cm^{-2}. The electrode was dried in air for 30 mins followed by vacuum drying at 50 ºC for 1 h. Circular cathodes were punched from the electrode film with an area of 1.33 cm^2 before transfer into a glove box filled with argon (<1 ppm H_2O and O_2). Li foil was used as an anode and Celgard 2325 as separator, where the anode and separator were punched into circles with an area of 1.60 cm^2 and 1.98 cm^2, respectively. 1.2 M $LiPF_6$ in 3:7 ethylene carbonate:ethyl methyl carbonate (Gotion) was used as the electrolyte. The components were assembled into coin cells (2032-type) in the glove box and then evaluated electrochemically using a multichannel battery cycler (MACCOR) with a voltage range of 3.5 V to 4.3 V (vs. Li/Li^+). Charge/discharge rates used for cycling were on a C rate basis, where 1C was calculated assuming 148 mA g^{-1} of cathode active material, and the indicated rate was used for both charge and discharge for a given cycle.

For sintered electrode cells, electrodes were processed by first mixing the electroactive material with a 1 wt% polyvinyl butyral (PVB) solution (Pfaltz & Bauer) in ethanol with a ratio of 1 g powder per 2 mL solution. The suspension was rigorously blended by hand using mortar and pestle and allowed to dry in air. Note that for sintered cathodes LMO (pristine or doped with the various amounts of Cu or Al) was used as the electroactive material, where for the sintered anodes $Li_4Ti_5O_{12}$ (LTO, NEI corporation) was used. Detailed characterization of the LTO material, including in sintered electrode electrochemical systems, can be found in previous reports [8,10,11]. 0.2 g of PVB-coated powder was then loaded into a circular pellet die (Carver) with an area of 1.33 cm^2 and pressed at 420 MPa for 2 mins with a hydraulic press (Carver). The pressed pellet was transferred into a box furnace and heated to 700 ºC for 1 h for LMO (pristine or doped), and 600 ºC for 1 h for LTO, where the ramp rate to the set temperature was 1 ºC min^{-1}. After the hold, the furnace was cooled to 30 ºC at a rate of 1 ºC min^{-1}. Final pellet loadings ranged from 140 – 150 mg cm^{-2} and geometric void/porosity volume fractions were 0.31–0.35 for cathode and 0.39–0.41 for anode after heat treatment. LMO and LTO pellets were adhered to the bottom plate and the spacer of the 2032-type cell, respectively, using a customized carbon paste with mass ratio of 1:1 CB:PVP dissolved in ethanol, where the PVP was dissolved at a 5 wt% concentration in ethanol. The pellets attached to the cell components were dried in air for 30 mins followed by vacuum drying at 50 ºC for 1 h before transfer to the glove box. 1.2 M $LiPF_6$ in 3:7 ethylene carbonate:ethyl methyl carbonate (Gotion) was used as electrolyte, and glass fiber (Fisher, type G6 circles) was used as separator. The coin cells containing sintered electrodes were evaluated electrochemically using a multichannel battery cycler (MACCOR) with a voltage range of 2.0 V to 2.8 V (cell voltage), where 1C was calculated assuming 148 mA g^{-1} of cathode active material, and the indicated rate was used for both charge and discharge for a given cycle.

2.3. Material characterization

Scanning electron micrographs (SEM) were conducted on powders and pellets using a FEI Quantum 650. Powder x-ray diffraction (XRD) patterns for powders were collected using a PANalytical X'pert ProMPD. Rietveld refinements on XRD patterns were performed using FullProf Suite [46,47]. To determine geometric porosity/void volume fraction, the crystal density was determined from XRD refined parameters which was combined with the measured solid material mass to calculate the solid material volume, and geometric measurements of the pellets with calipers were used to determine the total pellet volume.

For direct current (DC) conductivity measurements, the as-sintered pellets were coated with silver paste (Sigma-Aldrich) and dried at 80 ºC for 20 min. The coated pellets were sandwiched between two stainless steel spacers with diameter of 16 mm and thickness of 0.5 mm, with pressure applied via a clamp. Gamry Reference 600 was used to provide a constant voltage at 10 mV and currents were recorded to calculate the pellet conductivity. The measured conductivities for the pellets were then adjusted by the porosity and tortuosity of the pellet to calculate the material conductivity, where a Bruggeman exponent of 1.5 was assumed [4].

3. Results and discussions

3.1. Undoped and doped LMO material characterization

The precipitation process for producing the $MnC_2O_4 \cdot 2H_2O$ has been described previously in detail, and results in particles with a secondary morphology with a platelet structure [45,48]. During the calcination process, water was removed from the structure and the oxalate decomposed to a metal oxide which subsequently reacted with lithium to produce the final active material [44,45,49]. The oxalate decomposition and water removal resulted in porous aggregates of primary particles with polydisperse dimensions, although most were between a few hundred nanometers and a couple of micrometers in length (for SEMs of the morphology of active materials particles of pristine, Al-doped, and Cu-doped LMO compositions, see Supporting Information, Figure S1). All the pristine, Al-doped and Cu-doped LMO materials had similar primary particle morphology. When processing into sintered electrodes, the powders were hydraulically pressed, resulting in the secondary particles being forced together and the loss of being able to distinguish secondary particle morphologies. The sintering treatment was relatively mild, however, and the primary particle sizes did not undergo noticeable increase in size – although the hydraulic pressing process makes distinguishing between primary particle boundaries more challenging (for SEMs of the active material powders after hydraulic compression and thermal treatment see Supporting Information, Figure S2). Primary particle sizes based on the averages of 20 randomly selected particles for each material can be found in Supporting Information, Figure S3. The Al-doped samples exhibited slightly smaller average particle sizes, but it is noted that the standard deviations for the particle sizes were relatively large. All materials had average primary particle sizes that fell within a range of 0.5 µm to 1.5 µm, and it was not expected that variations within this size range impacted the electrochemical outcomes for the sintered electrodes, especially when cycling at relatively slow C-rates.

The resulting solid electroactive materials, including pure LMO and all Cu and Al doping levels investigated, had no noticeable impurities from the XRD patterns (patterns can be found in Supporting Information, Figure S4). All materials were consistent with the *Fd-3 m* spinel structure [50]. Substitution of Mn with Al or Cu resulted in a decrease in the refined lattice parameter *a*, as shown in Fig. 1. In this report, the composition will be referred to as

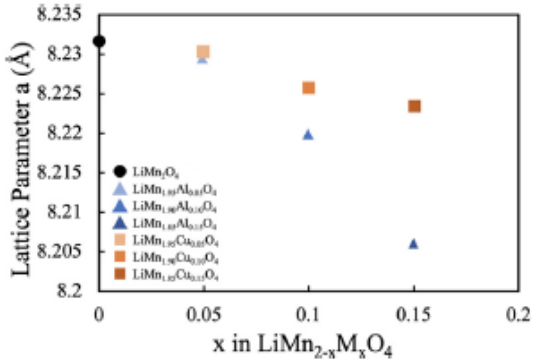

Fig. 1. Lattice parameters determined from refinement of powder XRD patterns for $LiMn_{2-x}M_xO_4$ materials, where x ranged from 0 to 0.15. The materials evaluated were $LiMn_2O_4$ (black circle), $LiMn_{1.95}Al_{0.05}O_4$ (light blue triangle), $LiMn_{1.90}Al_{0.10}O_4$ (blue triangle), $LiMn_{1.85}Al_{0.15}O_4$ (dark blue triangle), $LiMn_{1.95}Cu_{0.05}O_4$ (light orange cube), $LiMn_{1.90}Cu_{0.10}O_4$ (orange cube), and $LiMn_{1.85}Cu_{0.15}O_4$ (dark orange cube).

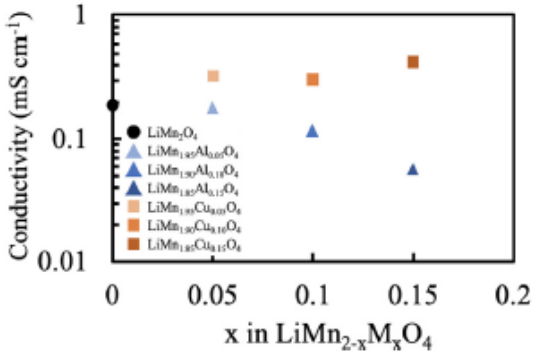

Fig. 2. Electronic conductivities determined from DC measurements for $LiMn_{2-x}M_xO_4$ materials, where x ranged from 0 to 0.15. The materials evaluated were $LiMn_2O_4$ (black circle), $LiMn_{1.95}Al_{0.05}O_4$ (light blue triangle), $LiMn_{1.90}Al_{0.10}O_4$ (blue triangle), $LiMn_{1.85}Al_{0.15}O_4$ (dark blue triangle), $LiMn_{1.95}Cu_{0.05}O_4$ (light orange cube), $LiMn_{1.90}Cu_{0.10}O_4$ (orange cube), and $LiMn_{1.85}Cu_{0.15}O_4$ (dark orange cube).

$LiMn_{2-x}M_xO_4$, where $x = 0$ is pure LMO and for other x values that is the stoichiometry of the dopant M, where M is either Al or Cu. The ionic radii for Al^{3+}, Cu^{2+}, Mn^{3+}, and Mn^{4+} are 67.5, 73, 78.5, and 67 pm, respectively [51,52]. For Al substituted samples, the Al was expected to be Al^{3+} and directly replace Mn^{3+} in the spinel structure. Thus, the observed smaller lattice parameter for increasing Al doping was consistent with the smaller size of Al^{3+} in the structure relative to Mn^{3+}. For Cu^{2+} doped samples, every Cu^{2+} substituted into the structure would result in an additional Mn^{4+} from Mn^{3+} relative to the undoped LMO material. Thus, increased Cu doping would also be expected to reduce the lattice parameter, and this reduction was also observed – although at the higher dopant extents the Al doping caused greater reductions in the lattice parameter relative to the Cu substitutions. Both trends for the lattice parameter with Al or Cu substitution were consistent with previous reports [51,53,54].

Electronic conductivity for the sintered electrodes of all compositions using DC conductivity measurements can be found in Fig. 2. The undoped LMO had a measured electronic conductivity of 1.9×10^{-4} S cm^{-1}, which was within the range of previous reports [22,23,25,55–57]. For Al doping, with increasing Al concentration from Al = 0 to Al = 0.15, the conductivity dropped by ~76%, and this trend was consistent with previous literature as well [58]. The electronic conduction in LMO has been reported to be due primarily to the hopping of charge carriers, via electrons in the 3d e_g orbital of Mn^{3+} between the Mn^{3+} and Mn^{4+} in the spinel structure [57,59]. Even though doping contracted the lattice which could be favorable for electron hopping, the vacant 3d orbitals due to doping could have made electron hopping across the 16d sites

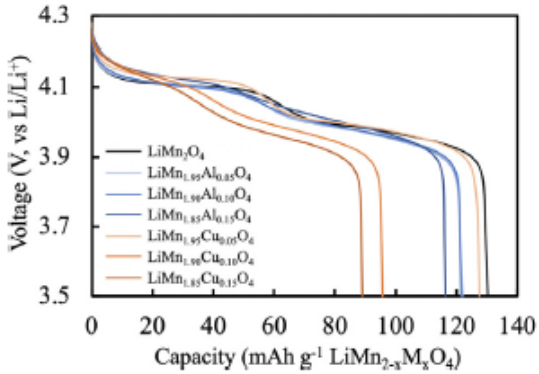

Fig. 3. Voltage profiles of first discharge at C/20 for $LiMn_{2-x}M_xO_4$ materials in composite electrode paired with Li foil anode, where x ranged from 0 to 0.15. The materials evaluated were $LiMn_2O_4$ (black), $LiMn_{1.95}Al_{0.05}O_4$ (light blue), $LiMn_{1.90}Al_{0.10}O_4$ (blue), $LiMn_{1.85}Al_{0.15}O_4$ (dark blue), $LiMn_{1.95}Cu_{0.05}O_4$ (light orange), $LiMn_{1.90}Cu_{0.10}O_4$ (orange), and $LiMn_{1.85}Cu_{0.15}O_4$ (dark orange). The initial charge was also at C/20.

more difficult [58]. In addition, Al^{3+} replacement likely reduced the amount of charge carriers in the 3d e_g orbital, which could have caused decreased electronic conductivity [57]. For Cu doping, the electronic conductivity increased by ~30% from Cu = 0 to Cu = 0.15, with the increasing conductivity at increased Cu dopant concentrations also consistent with previous reports [23,24]. Cu^{2+} has 9 electrons in the 3d orbital (with one more to fully fill the orbital), making it an excellent receiver of electrons [23,24]. Since LMO is a n-type semiconductor, Mn^{3+} replacement by Cu^{2+} with lower 3d states than that of Mn could provide 3d valence e_g holes for e_g electrons from Mn^{3+} to facilitate charge transport, enhancing electronic conductivity [23,24,60–62]. Another possible supporting perspective is the total electron density of states (DOS) from first principle calculation by Liu et al. [60], which demonstrated that the Cu substitution could effectively shift the 3d contribution/partial DOS above the Fermi level to the lower energy region, and an additional peak appeared below the Fermi level. Thus, the band gap between the conduction band and valence band was shortened, improving the electronic conductivity.

3.2. $LiMn_{2-x}M_xO_4$ electrochemical evaluation in composite electrodes

Before analysis of sintered electrodes comprised of only the electroactive materials, the cathode materials were evaluated in composite electrodes. The composite electrodes contained carbon black, and thus electronic conductivity through the electrode matrix was not expected to have a major impact on electrochemical properties and would enable evaluation of the intrinsic electrochemical capacity of the materials. The first discharge voltage profiles for composite electrodes containing the different active materials at a rate of C/20 can be found in Fig. 3. The dopant-free LMO had the largest capacity of 130 mAh g^{-1}, with two distinct voltage plateaus at ~ 4.04 V and ~ 4.15 V associated with a single phase reaction between $LiMn_2O_4$ and $Li_{0.5}Mn_2O_4$ and a two-phase reaction between $Li_{0.5}Mn_2O_4$ and λ-MnO_2 [63,64].

With increasing Al dopant concentration, the discharge capacity decreased, which was consistent with previous reports [54,65]. The Al remained in the 3^+ oxidation state and did not participate in redox chemistry. Thus, every Mn^{3+} substituted for Al^{3+} was a loss of a Mn^{3+} that cannot be oxidized to Mn^{4+} during charge (and reversibly reduced back to Mn^{3+} during discharge). The capacity lost for each Mn^{3+} substitution may not exactly match experimental outcomes due to other factors such as defects in the structure, however, the general trend of decreasing capacity with increasing Al^{3+} was observed. Discharge capacity from rate capability testing of the composite electrodes can be found in Supporting Information, Figure S5. The LMO had higher capacity retention at increasing rates up to 1C compared to any of the Al-doped materials. However, there was capacity fade for the LMO cell, which resulted in the $LiMn_{1.9}Al_{0.1}O_4$ sample having greater capacity than the dopant-free LMO after returning to the slower C/20 rate after the tests at increasing rates. The capacity retention for the last (40th) cycle increased as the Al dopant concentration increased (Fig. 4a). It is noted that although Al has been reported to reduce the electronic conductivity of LMO, it has also often been added as a dopant in order to suppress the onset of Jahn-Teller distortion which can result in capacity fade [36]. In some cases Al doping can also mitigate Mn dissolution into the electrolyte [66,67]. In general, Al doping was consistent with previous reports of LMO in composite electrodes where doping with Al reduces initial electrochemical capacity but aids in retaining capacity with cycling [54,65].

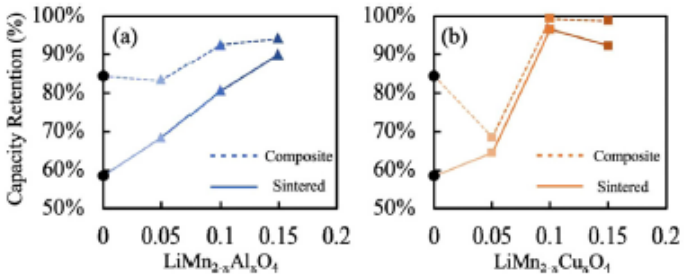

Fig. 4. Capacity retention (based on first discharge capacity) of last cycle of rate capability testing for Al-doped LMO (a) and Cu-doped LMO (b) in both sintered electrodes at C/50 (solid) and composite electrode at C/20 (dashed).

With increasing Cu dopant concentration, the capacity decreased more than that of Al-doped materials. Due to the relatively low concentration in this study, the majority of the Cu doped into the LMO crystal was expected to have an oxidation state of 2^+, resulting in even less available Mn^{3+} than that of Al-doped materials [39,68–70]. Further oxidation of Cu^{2+} to Cu^{3+} at ~ 5 V was not investigated in this study [31,38]. The capacity loss was not strictly linear per Cu substitution, likely due to other factors such as defects, tetrahedral sites (8a) occupied by Cu (ideally tetrahedral sites (8a) are occupied by Li and octahedral sites (16d) by Cu/Mn), and the presence of other Cu oxidation states [52,68,69,71]. At high charge/discharge rate, the capacity retention of $LiMn_{1.95}Cu_{0.05}O_4$ was the best among all materials, but at even higher Cu concentration rate capability declined. Due to the creation of Mn^{4+} by Cu^{2+} substitution, Jahn-teller may be suppressed as would be expected for Al dopants [72]. First principles calculations have also suggested that Cu doping can alleviate Mn dissolution as well [73]. Both $LiMn_{1.9}Cu_{0.1}O_4$ and $LiMn_{1.85}Cu_{0.15}O_4$ had almost complete capacity retention on the final cycle of the rate capability testing, although the capacity retention for $LiMn_{1.95}Cu_{0.05}O_4$ was not as high as pristine LMO.

3.3. $LiMn_{2-x}M_xO_4$ electrochemical evaluation in sintered electrodes

Without the electronic conductivity from carbon black in the composite, sintered electrodes comprised of $LiMn_{2-x}M_xO_4$ materials relied on electronic conduction though the active material itself for transport of electrons through the electrode matrix. Note that, for sintered electrodes, the C-rate was still based on the mass of cathode material but with much larger areal loadings (~ 150 mg cm^{-1}) compared to that of the composite electrodes (< 10 mg cm^{-1}). Thus, the current densities at C/20 for composite electrodes were more than one order of magnitude smaller than those at C/20 for sintered electrodes. According to a prior modeling report, at C/50 and C/20 cycle rates the electrolyte concentration gradient was mild and the ionic overpotential was too small

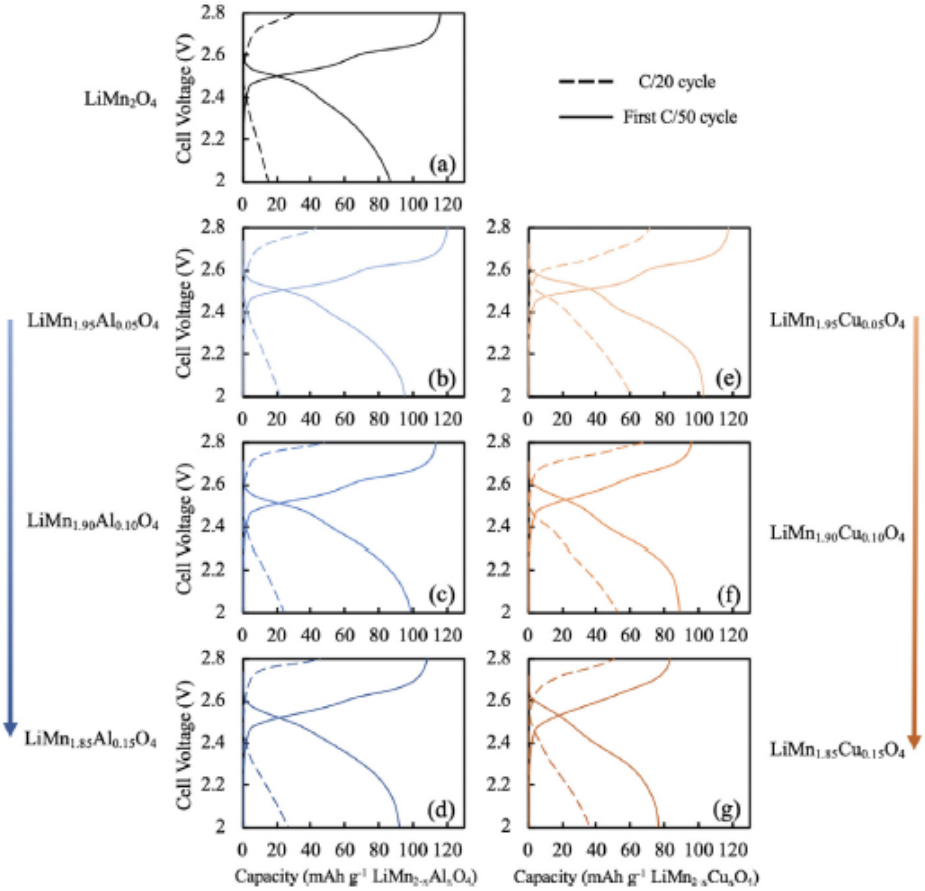

Fig. 5. Voltage profiles of first cycle at C/50 (solid) and C/20 (dashed, after five C/50 cycles) for $LiMn_{2-x}M_xO_4$ materials in sintered electrode paired with sintered LTO anode, where x ranged from 0 to 0.15. The materials evaluated were $LiMn_2O_4$ (a, black), $LiMn_{1.95}Al_{0.05}O_4$ (b, light blue), $LiMn_{1.90}Al_{0.10}O_4$ (c, blue), $LiMn_{1.85}Al_{0.15}O_4$ (d, dark blue), $LiMn_{1.95}Cu_{0.05}O_4$ (e, light orange), $LiMn_{1.90}Cu_{0.10}O_4$ (f, orange), and $LiMn_{1.85}Cu_{0.15}O_4$ (g, dark orange). Charge and discharge were conducted at the same rate.

to limit the electrochemical capacity of the cells with sintered electrodes with similar dimensions to those in this study [11].

Pristine LMO: The voltage profiles for the first charge and discharge cycles at C/50, and the first charge and discharge cycles at C/20 (the 6th cycle of a rate capability test where the first 5 charge/discharge cycles were at C/50) for pristine, Cu-doped, and Al-doped materials can be found in Fig. 5. All cells were cathode limited in capacity and paired with nominally identical sintered LTO anodes. For pristine LMO at C/50, the first discharge capacity was 86 mAh g^{-1} LMO, much less than composite electrodes (130 mAh g^{-1} LMO), and the capacity loss between the first charge and discharge was quite large (29 mAh g^{-1} LMO for the sintered electrode, and 4 mAh g^{-1} LMO for the composite electrode). During the charge cycle, two voltage plateaus were present, however they had significant slopes and were not as flat as the composite electrode profiles – even though with the LTO anode in the absence of polarization the charge profiles would still be expected to have flat plateaus [66]. Moreover, during even the initial discharge cycle at the low rate of C/50, an initial more plateaued voltage region at ~2.5 V was observable, but the second capacity plateau had declined severely. At C/20, the capacity was less than 20 mAh g^{-1} LMO, and there was almost no capacity at a rate of C/10. The discharge capacities during rate capability evaluation of pristine, Al-doped, and Cu-doped LMO materials as sintered electrodes can be found in Supporting Information, Figure S6.

Despite the low electronic conductivity of pristine LMO sintered electrodes, previous reports have indicated that the electronic conductivity of LMO has dependence on the extent of lithiation, and that LMO has increased conductivity when delithiated [25,55,60,74,75]. The increased conductivity with oxidation of the Mn and removal of Li^+ has been attributed to the amount of the charge carrier (Mn^{3+} electrons) and the hopping distance between the Mn-Mn [76,77]. Upon delithiation, Nishizawa et al. [57] proposed that the net conductivity change was from the competition between the shortened hopping distance (increasing conductivity) between Mn-Mn and fewer charge carrier Mn^{3+} (decreasing conductivity); the two-phase transition between $Li_{0.5}Mn_2O_4$ and λ-MnO_2 provided a conduction path of shortened Mn-Mn from the λ-MnO_2 phase and charge carriers from the $Li_{0.5}Mn_2O_4$ phase. As a result, qualitative analysis of an outcome of the electronic conductivity change was performed by comparing the two Δ dQ/dV peak positions of both sintered (vs LTO) and composite (vs Li foil) cells. The initial charge cycles were used for the analysis to exclude capacity fading issues (arising from Jahn-Teller distortion and/or Mn dissolution [66,78–80]), and with an aim to reflect the overpotential differences solely from the electrode electronic conductivity. The Δ dQ/dV peak positions were calculated as described in the following. Composite dQ/dV peak positions were extracted from the initial C/20 charge [81], where it was assumed there was minimal polarization at this low rate for composite electrodes and any changes in open circuit voltages due to doping were accounted for by only comparing the same materials used in composite and sintered electrodes. Sintered electrode cell dQ/dV peak positions were then extracted and had a value of 1.56 V added to them. This addition accounted for the sintered electrode cells having LTO anodes, where 1.56 V was the difference between the LTO plateau region open circuit voltage (OCV) and Li/Li^+ [82]. Sintered LTO electrodes have a flat OCV as a function of lithiation and high conductivity above ~10^2 S m^{-1} in the lithiation range during most of the charge cycle (~95% of the LTO) [83]. The Δ dQ/dV value was

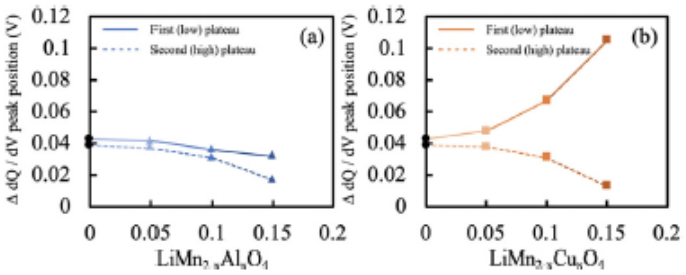

Fig. 6. First (solid) and second (dashed) Δ dQ / dV peak positions of the first charge cycle for Al-doped LMO (a) and Cu-doped LMO (b) in sintered electrode cells at C/50.

then the difference between the composite material dQ/dV peak position and the adjusted dQ/dV peak position (by LTO OCV) for a sintered electrode of the same material. It was expected that decreased electronic conductivity for an electroactive material would then result in an increase in the Δ dQ/dV value for a material. The Δ dQ/dV peak position associated with the first plateau during charge (at the lower potential) was observed to be greater than the second (Fig. 6). Assuming that this difference was due to the electronic conductivity of the electroactive material (at the slow charge/discharge rate the more common major contributor to polarization of ion transport through the microstructure was not expected to contribute significantly [9,11,84]), this result would indicate that the single phase reaction transition ($LiMn_2O_4/Li_{0.5}Mn_2O_4$) had a lower electronic conductivity than the two-phase transition ($Li_{0.5}Mn_2O_4/\lambda$-MnO_2). Such observation was consistent with the observed voltage curve polarization and the offsets between the first charge and discharge capacities at C/50.

Although direct comparison between the last cycle discharge capacity retention between the composite and sintered cells would be inappropriate because of the significant difference in relative charge/discharge capacities, cycling rates, current densities, and state of charge experienced by the cells, the last cycle retention of capacity of sintered cells relative to the first cycle still may provide insights into the conductivity changes during cycling. For dopant-free LMO the capacity retention for the final cycle was 84% for the composite electrode, but only 58% was achieved for the sintered electrode. The first cycle coulombic efficiencies (CE) of sintered and composite cells were ~75% and ~97%, respectively (see Supporting Information, Figure S7). In examining the dQ/dV plots for the first two charge cycles (Fig. 7a), the lower voltage peak had decreased intensity on the second cycle, which likely originated due to the undischarged capacity from previous discharge cycle, which may have been due to the variable (and reduced) conductivity described earlier. Both dQ/dV peak positions from the charge process shifted towards higher voltage on the second cycle relative to the first, suggesting an increased overall resistance in addition to the lithiation-dependent electronic conductivity. It was speculated that these results were caused by either: (i) the sintered electrode had much greater active material surface area than that of composite electrode, and thus Mn dissolution caused by HF attack [67] was more severe, or (ii) during discharge, the Jahn-Teller distortion resulted in tetragonal phase formation at the surface of the electrode material in the operating voltage above ~ 3.5 V [78–80], which would have orders of magnitude lower electronic conductivity than the pristine spinel phase [36,43,72,85–87]. Thus, during discharge, the electronic conductivity of LMO could be even lower, compared to the charge process, collectively from both the Jahn-Teller distortion and lithiation dependent electronic conductivity mentioned above [55].

Al-doped LMO: For all Al-doped LMO sintered electrodes, the first C/50 discharge capacities were greater than that of pristine LMO, and the irreversible first cycle capacity loss between charge and discharge was much smaller (Figs. 5b-d). At C/20 charge/discharge rate, the discharge capacities were slightly greater than 20 mAh g^{-1}, which were slightly greater than that of the pristine LMO. When looking at the Δ dQ/dV peak positions, with increasing Al concentration, both peaks, especially the second peak associated with the higher voltage charging plateau, shifted to lower differences (Fig. 6a), suggesting a lithiation dependent electronic conductivity where the Al-doped LMO became more electronically conductive during delithiation relative to pristine LMO. It was possible that increased electronic conductivity during the two-phase transition relative to pristine LMO originated from the contracted crystal lattice resulting from the Al doping. Al-doped LMO exhibits two-phase features (the presence of both $Li_{0.5}Mn_2O_4$ phase to provide charge carriers and λ-MnO_2 phase to provide shortened electron hopping distance) during charge similar to pristine LMO [23,24,42,57,60,88], and upon delithiation the Mn-Mn distance would be further shortened compared to the pristine LMO due to the lattice contraction from Al substitution. The competition between charge carriers and hopping distance was likely dominated by the latter despite the reduced charge carriers due to the replacement of Mn^{3+} by Al^{3+}. Thus, even though the original sintered electrode Al-doped materials had lower electronic conductivity than that of pristine LMO, the higher capacity, first cycle CE, capacity retention, and rate capability of the same Al-doped electrodes may have resulted due to the increased electronic conductivity after the material started the delithiation process.

As the Al concentration was increased for the Al-doped LMO sintered electrodes, the capacity retention for the last cycle in the rate capability experiments increased (Fig. 4a). As mentioned before, it was speculated that the inhibited Jahn-Teller distortion and Mn dissolution processes resulted in capacity retention increasing from 58% to 89% for $LiMn_2O_4$ compared to $LiMn_{1.85}Al_{0.15}O_4$. The first cycle CEs of the composite cells did not change much (± 1%), but the sintered cells had noticeable improvement and reached 87% first cycle coulombic efficiency for $LiMn_{1.9}Al_{0.1}O_4$ compared to 75% without doping (Supporting Information, Figure S7). When looking at the dQ/dV plots for the first two cycles (Figs. 7b-d), decreases in the intensity of the first (lower voltage) charge peak intensity was mitigated with increasing Al concentration. This could be explained by the increased electronic conductivity in the lower voltage plateau region because during the previous discharge cycle greater electronic conductivity would allow greater extents of lithiation and more delivered capacity. The shifting of both dQ/dV charge peaks towards higher voltage, which was an indicator of increased overall polarization discussed above, was slightly suppressed possibly from the inhibition of Mn dissolution and Jahn-Teller distortion [36,54,65–67].

Cu-doped LMO: The Cu-doped LMOs had the smallest irreversible first cycle capacity loss between the first charge and discharge cycles among pristine, Al-doped, and Cu-doped samples in this study (Figs. 5e-g). $LiMn_{1.95}Cu_{0.05}O_4$ had the greatest initial C/50 discharge capacity of over 100 mAh g^{-1} and achieved ~ 60 mAh g^{-1} at C/20. When looking at the Δ dQ/dV peak positions (Fig. 6b), the first (lower voltage) peak shifted to increased values while the second (higher voltage) peak shifted towards decreased values. This result indicated that as Cu concentration increased the electronic conductivity of the single-phase transition decreased while the two-phase transition increased. The conductivity decrease in the single-phase transition was contrary to the pristine and Al-doped LMO, which may have been due to the reduction of charge carriers (two Mn^{3+} were lost for every one Cu^{2+} doped). Also, compared to substitution with Al^{3+} the cell contraction was not as pronounced suggesting the competition between expected factors that influenced the conductivity was dominated by the number of charge carriers rather than the mildly

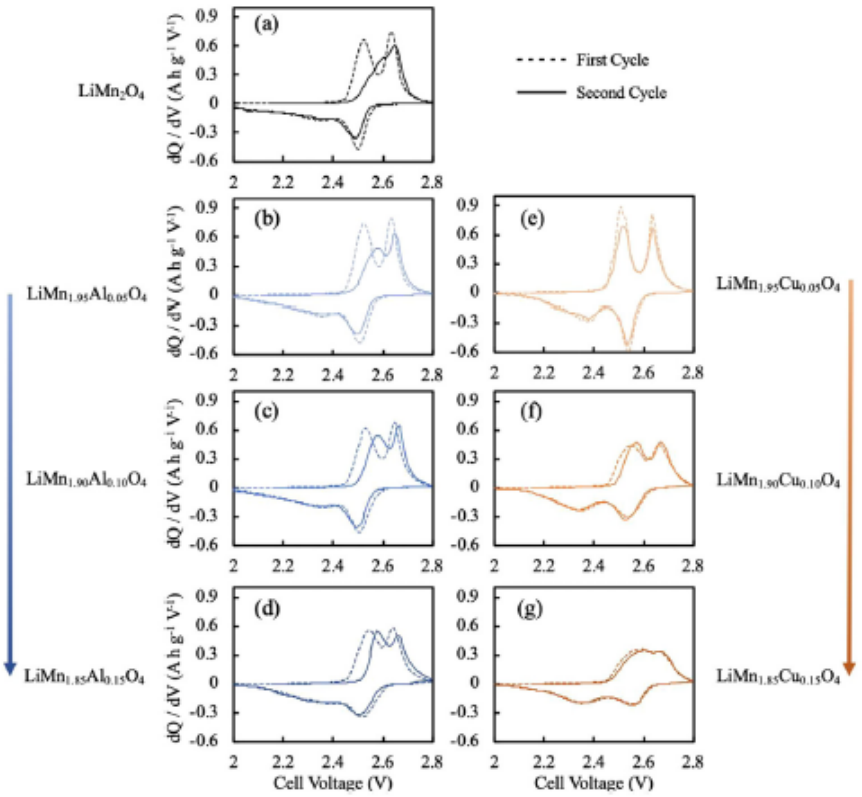

Fig. 7. First (solid) and second (dashed) cycle dQ/dV profiles at C/50 for $LiMn_{2-x}M_xO_4$ materials in sintered electrode paired with sintered LTO anode, where x ranged from 0 to 0.15. The materials evaluated were $LiMn_2O_4$ (a, black), $LiMn_{1.95}Al_{0.05}O_4$ (b, light blue), $LiMn_{1.90}Al_{0.10}O_4$ (c, blue), $LiMn_{1.85}Al_{0.15}O_4$ (d, dark blue), $LiMn_{1.95}Cu_{0.05}O_4$ (e, light orange), $LiMn_{1.90}Cu_{0.10}O_4$ (f, orange), and $LiMn_{1.85}Cu_{0.15}O_4$ (g, dark orange).

reduced hopping distance. Thus, for the Cu-doped materials the more electronically conductive pathways were not available until the two-phase reaction. Once the reaction proceeded to the two-phase transition, a strong decreasing trend of Δ dQ/dV peak positions was observed with increasing Cu content. This indicated the greatest electronic conductivity increase occurred in the two-phase transition region. The increased electronic conductivity may be explained from the creation of pathways for electron hopping from the contracted cell lattice, supported by DOS calculations from Liu et al. using first principles [60] which found an even shorter band gap between the conduction band and valence band after delithiation [23,24,57,60].

In summary, the Δ dQ/dV analysis suggested the electronic conductivity of Cu-doped LMO upon delithiation decreased until the two-phase transition, and then increased relative to pristine LMO. Such conductivity trends agreed with the charging voltage profiles at C/20 (Fig. 5e-g), where the lower voltage plateau regions kept shifting upwards indicating increased polarization as the Cu concentration increased. For $LiMn_{1.95}Cu_{0.05}O_4$ the low voltage plateau initiated at ~ 2.6 V, and two voltage plateaus were observable; for the $LiMn_{1.9}Cu_{0.1}O_4$ the charge process initiated at ~ 2.7 V and the higher voltage plateau was not as wide of a capacity region; for the $LiMn_{1.85}Cu_{0.15}O_4$ the charge processes initiated over ~ 2.7 V and there was not a clear higher voltage plateau. Even though $LiMn_{1.9}Cu_{0.1}O_4$ already proceeded to the higher conductivity region at the higher voltage plateau, the plateau capacity was reduced and the curve was sloped. This was rationalized by the observation that the Δ dQ/dV decreased at the higher voltage plateau region (~ 10 mV), but the dQ/dV higher voltage peak for the composite electrode had increased (~ 35 mV, shown in Supporting Information, Figure S8). Thus, although the Δ dQ/dV indicated improved conductivity, the redox potential for the material had shifted to a higher voltage and thus less capacity was accessible for the same cutoff voltage at 2.8 V. The sharp increase in the dQ/dV peak positions at Cu = 0.10 could have resulted from increased relative Cu substitution at the Mn site (16d) relative to the Li site (8a) for the increase in total Cu doping [52]. If that occurred, it could account for the shift in the dQ/dV peak position in the composite electrode. As a result, the $LiMn_{1.95}Cu_{0.05}O_4$ delivered the greatest capacity since it was least affected by the electronic conductivity of the lower voltage plateau and because the voltage for oxidizing the material was intrinsically lower compared to the higher Cu substituted materials, enabling more capacity to be extracted during the charge cycle because the same cutoff voltage was always applied.

When looking at the retention of capacity of the last cycle from the rate capability analysis of the sintered electrodes (Fig. 4b), the Cu-doped LMOs generally had improved stability relative to pristine LMO. For example, the $LiMn_{1.9}Cu_{0.1}O_4$ retained over 96% of its initial discharge capacity, the best retention among pristine, Al-doped, and Cu-doped sintered electrodes. The $LiMn_{1.95}Cu_{0.05}O_4$ had little improvement relative to pristine LMO possibly due to the Cu being substituted into the 8a position at higher relative amounts to 16d positions at that level of substitution. $CuMn_2O_4$ may not have reduced the Jahn-Teller impacts and Mn dissolution which was also likely the source of lower capacity retention for unsubstituted $LiMn_2O_4$. Compared to Al-doped materials, the first cycle CEs of Cu-doped materials improved notably and reached a maximum at $LiMn_{1.9}Cu_{0.1}O_4$ with 93% (Supporting Information, Figure S7). In examining the dQ/dV of the first two cycles, the lower voltage peak from dQ/dV during the charge cycle had less of a decrease in intensity from the first to the second cycle for the Cu-doped materials relative to the Al-doped materials (Fig. 7). The retention of the intensity of the first charge peak was despite the lower conductivity of the Cu-doped materials for the first plateau region during charge (inferred from the results in Fig. 6). One explanation for this

outcome was that the Al-doped materials were unable to fully discharge their capacity. The dQ/dV plots (Fig. 7) suggested that the differential capacity was approximately zero well before the lower cutoff voltage for the Cu-doped materials, but had not reached zero for the Al-doped materials. This may have been due to the lower conductivity for Al-doped materials relative to Cu-doped materials as they approach full lithiation (Fig. 2), which could be another cause to the improvement in the first cycle CEs (Supporting Information, Figure S6). Also, compared to the Al-doped materials, the dQ/dV peak shift between the first two cycles decreased significantly with increasing Cu doping levels (Fig. 7e-g), which may have been due to the suppression of Jahn-Teller distortion and/or Mn dissolution with increasing Cu substitution [72,73].

3.4. Al and Cu co-doped $LiMn_{2-x-y}Al_xCu_yO_4$ characterization and electrochemical evaluation

Motivated by combining the merits of both Al and Cu doping, Al and Cu co-doped materials were also explored. No obvious impurity peaks appeared in the XRD patterns for these materials (see Supporting Information, Figure S4). The refined lattice parameters can be found in Supporting Information, Figure S9. All the co-doped materials demonstrated smaller lattice parameters relative to pristine LMO, similar to observations for the materials doped with Al or Cu in isolation. $LiMn_{1.85}Al_{0.10}Cu_{0.05}O_4$ had a slightly smaller lattice parameter than that of $LiMn_{1.85}Al_{0.05}Cu_{0.10}O_4$, which followed the trend where at the same level of dopant concentration, the Al doping had a smaller lattice parameter than Cu doping. Interestingly, the $LiMn_{1.90}Al_{0.05}Cu_{0.05}O_4$ and $LiMn_{1.85}Al_{0.10}Cu_{0.05}O_4$ had the smallest lattice parameter among the materials with dopant concentrations of 0.10 and 0.15, which may have been due to other factors such as crystal defect densities or inhomogeneous distribution of two dopants. As for electronic conductivities, a trend was observed where electronic conductivity increased with additional Cu and decreased with additional Al. All co-doped materials contained Cu, however, and correspondingly all co-doped materials had greater electronic conductivity than pristine LMO (see Supporting Information, Figure S10).

For the composite electrode evaluations, as the total doping concentration increased for co-doped materials, the discharge capacity decreased as expected and discussed earlier. The first discharge voltage curves can be found in Supporting Information, Figure S11. All co-doped samples exhibited more sloped voltage curves, which was more similar to the Cu-doped materials, and consistent with previously reported Al and Cu co-doped electrochemical data [89]. $LiMn_{1.90}Al_{0.05}Cu_{0.05}O_4$ reached 119 mAh g^{-1}, which was slightly lower than $LiMn_{1.9}Al_{0.1}O_4$ (122 mAh g^{-1}) but higher than $LiMn_{1.9}Cu_{0.1}O_4$ (96 mAh g^{-1}). The $LiMn_{1.85}Al_{0.10}Cu_{0.05}O_4$ and $LiMn_{1.85}Al_{0.05}Cu_{0.10}O_4$ reached 100 mAh g^{-1} and 98 mAh g^{-1}, respectively, and qualitatively followed the trend seen for the individually doped samples that for the same amount of doping concentration, Cu doping decreased the capacity more than Al doping in composite electrodes. Rate capability tests can also be found in Supporting Information, Figure S12.

As for the sintered electrode cells, for the first discharge cycle at C/50 (Fig. 8), $LiMn_{1.90}Al_{0.05}Cu_{0.05}O_4$ reached 96 mAh g^{-1}, followed by $LiMn_{1.85}Al_{0.10}Cu_{0.05}O_4$ (90 mAh g^{-1}) and $LiMn_{1.85}Al_{0.05}Cu_{0.10}O_4$ (88 mAh g^{-1}). At C/20, $LiMn_{1.90}Al_{0.05}Cu_{0.05}O_4$ delivered 65 mAh g^{-1}, the best among all materials evaluated, followed by $LiMn_{1.85}Al_{0.10}Cu_{0.05}O_4$ (64 mAh g^{-1}) and $LiMn_{1.85}Al_{0.05}Cu_{0.10}O_4$ (57 mAh g^{-1}). Rate capability tests can also be found in Supporting Information, Figure S13. When looking at the Δ dQ/dV (see Supporting Information, Figure S14), the trend was similar to the Cu-doped samples where the Δ dQ/dV of second (high) voltage plateau increased as the dopant concentration increased. However,

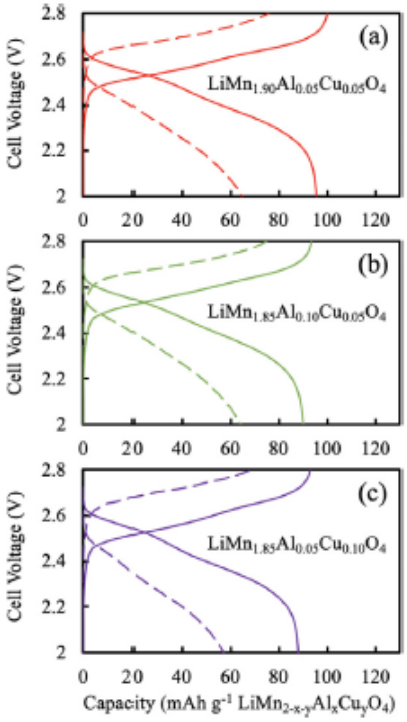

Fig. 8. Voltage profiles of first cycle at C/50 (solid) and C/20 (dashed, after five C/50 cycles) for $LiMn_{2-x-y}Al_xCu_yO_4$ materials in sintered electrode paired with sintered LTO anode. The materials evaluated were $LiMn_{1.90}Al_{0.05}Cu_{0.05}O_4$ (a, red), $LiMn_{1.85}Al_{0.10}Cu_{0.05}O_4$ (b, green), and $LiMn_{1.85}Al_{0.05}Cu_{0.10}O_4$ (c, purple). Charge and discharge were conducted at the same rate.

the magnitude of the increase was smaller than that of Cu-doped samples (Fig. 6), possibly originating from a combination between the Cu and Al, where the Al had an opposite decreasing trend for that peak with substitution (Fig. 6a). This improved electronic conductivity, coupled with the much smaller increase in second voltage plateau position (Supporting Information, Figure S15), were likely the major contributors to the greatest capacity being observed for $LiMn_{1.90}Al_{0.05}Cu_{0.05}O_4$ and $LiMn_{1.85}Al_{0.10}Cu_{0.05}O_4$ sintered electrodes. When looking at the retention of capacity of the last cycle from the rate capability analysis of the co-doped samples (Supporting Information, Figure S16), all co-doped materials in composite electrodes had retentions over 95%, and in the sintered electrodes had retentions over 93%. The first cycle CE of the co-doped materials in composite electrodes all exceeded 98%, and in sintered electrodes all exceeded 94%, the best among all materials evaluated (Supporting Information, Figure S17). In examining the dQ/dV of the first two cycles of the co-doped materials in sintered electrode, the dQ/dV change between the first two cycles was mitigated (Supporting Information, Figure S18). In summary, the co-doped materials had the most promising electrochemical properties of any of the materials evaluated when processed into sintered electrodes.

4. Conclusion

$LiMn_2O_4$ spinel materials, both undoped and doped with Al and Cu dopants to varying extents, were prepared and investigated as battery materials in sintered electrode architectures comprised of only electroactive material. Substitution of Mn with either Cu or Al decreased the lattice parameter of the crystal structure. For composite electrodes, increasing the dopant concentration decreased the available electrochemical capacity, which was attributed to the loss of Mn^{3+} in the structure. Consistent with previous reports in composite electrodes, Al substitution was found to improve the

material stability, while Cu substitution both improved stability and increased electronic conductivity of the pristine synthesized material. Sintered electrodes rely on electronic conduction through the active material itself, and thus limitations in electronic conductivity and stability were amplified in sintered electrodes relative to composite electrodes. The sintered electrodes were observed to have increases in both capacity retention and rate capability when doped with Al, and improvements in these electrochemical properties were even greater for Cu doping. Analysis of dQ/dV plots yielded insights into the impacts of the dopants on electronic conductivity. This study provides insights into how to improve the electrochemical cycling outcomes for materials with relatively low electronic conductivity when used as sintered electrodes comprised of only electroactive material. As alternatives to relatively high electronic conductivity materials such as $LiCoO_2$ are pursued, electronic conductivity and/or stability are likely to be a general challenge. Methods and analysis to improve sintered electrode material properties such as those reported herein will aid in making progress with these electrode configurations.

Declaration of Competing Interest

The authors declare that they have no known competing financial interests or personal relationships that could have appeared to influence the work reported in this paper.

Credit authorship contribution statement

Chen Cai: Conceptualization, Methodology, Investigation, Data curation, Writing – original draft. **Gary M. Koenig Jr.:** Conceptualization, Resources, Writing – review & editing, Supervision, Project administration, Funding acquisition.

Acknowledgements

The helpful suggestion of a reviewer to include Al and Cu co-doped materials in this report is acknowledged.

This research was funded by the National Science Foundation, grant CMMI-1825216.

Supplementary materials

Supplementary material associated with this article can be found, in the online version, at doi:10.1016/j.electacta.2021.139484.

References

[1] K.G. Gallagher, S.E. Trask, C. Bauer, T. Woehrle, S.F. Lux, M. Tschech, P. Lamp, B.J. Polzin, S. Ha, B. Long, Q. Wu, W. Lu, D.W. Dees, A.N. Jansen, Optimizing areal capacities through understanding the limitations of lithium-ion electrodes, J. Electrochem. Soc. 163 (2016) A138–A149 https://doi.org/, doi:10.1149/2.0321602jes.

[2] M. Ebner, D.W. Chung, R.E. García, V. Wood, Tortuosity anisotropy in lithium-ion battery electrodes, Adv. Energy Mater. 4 (2014) 1–6 https://doi.org/, doi:10.1002/aenm.201301278.

[3] M. Doyle, Comparison of modeling predictions with experimental data from plastic lithium ion cells, J. Electrochem. Soc. 143 (1996) 1890 https://doi.org/, doi:10.1149/1.1836921.

[4] B. Tjaden, S.J. Cooper, D.J. Brett, D. Kramer, P.R. Shearing, On the origin and application of the Bruggeman correlation for analysing transport phenomena in electrochemical systems, Curr. Opin. Chem. Eng. 12 (2016) 44–51 https://doi.org/, doi:10.1016/j.coche.2016.02.006.

[5] S. xue Yan, S. hua Luo, J. Feng, P. wei Li, R. Guo, Q. Wang, Y. hui Zhang, Y. guo Liu, S. Bao, Rational design of flower-like $FeCo_2S4$/reduced graphene oxide films: novel binder-free electrodes with ultra-high conductivity flexible substrate for high-performance all-solid-state pseudocapacitor, Chem. Eng. J. 381 (2020) 122695 https://doi.org/, doi:10.1016/j.cej.2019.122695.

[6] A. Abouimrane, O.C. Compton, K. Amine, S.T. Nguyen, Non-annealed graphene paper as a binder-free anode for lithium-ion batteries, J. Phys. Chem. C. 114 (2010) 12800–12804 https://doi.org/, doi:10.1021/jp103704y.

[7] Z.X. Huang, Y. Wang, Y.G. Zhu, Y. Shi, J.I. Wong, H.Y. Yang, 3D graphene supported MoO2 for high performance binder-free lithium ion battery, Nanoscale 6 (2014) 9839–9845 https://doi.org/, doi:10.1039/c4nr01744g.

[8] J.P. Robinson, J.J. Ruppert, H. Dong, G.M. Koenig, Sintered electrode full cells for high energy density lithium-ion batteries, J. Appl. Electrochem. 48 (2018) 1297–1304 https://doi.org/, doi:10.1007/s10800-018-1242-y.

[9] Z. Nie, S. Ong, D.S. Hussey, J.M. Lamanna, D.L. Jacobson, G.M. Koenig, Probing transport limitations in thick sintered battery electrodes with neutron imaging, Mol. Syst. Des. Eng. 5 (2020) 245–256 https://doi.org/, doi:10.1039/c9me00084d.

[10] Z. Nie, P. McCormack, H.Z. Bilheux, J.C. Bilheux, J.P. Robinson, J. Nanda, G.M. Koenig, Probing lithiation and delithiation of thick sintered lithium-ion battery electrodes with neutron imaging, J. Power Sources. 419 (2019) 127–136 https://doi.org/, doi:10.1016/j.jpowsour.2019.02.075.

[11] C. Cai, Z. Nie, J.P. Robinson, D.S. Hussey, J.M. LaManna, D.L. Jacobson, G.M. Koenig, Thick sintered electrode lithium-ion battery discharge simulations: incorporating lithiation-dependent electronic conductivity and lithiation gradient due to charge cycle, J. Electrochem. Soc. 167 (2020) 140542 https://doi.org/, doi:10.1149/1945-7111/abc747.

[12] R. Elango, A. Nadeina, F. Cadiou, V. De Andrade, A. Demortière, M. Morcrette, V. Seznec, Impact of electrode porosity architecture on electrochemical performances of 1 mm-thick LiFePO4 binder-free Li-ion electrodes fabricated by spark plasma sintering, J. Power Sources. 488 (2021) https://doi.org/, doi:10.1016/j.jpowsour.2020.229402.

[13] J. Li, T. Zhang, C. Han, H. Li, R. Shi, J. Tong, B. Li, Crystallized lithium titanate nanosheets prepared: via spark plasma sintering for ultra-high rate lithium ion batteries, J. Mater. Chem. A. 7 (2019) 455–460 https://doi.org/, doi:10.1039/c8ta10680k.

[14] B. Delattre, R. Amin, J. Sander, J. De Coninck, A.P. Tomsia, Y.-.M. Chiang, Impact of pore tortuosity on electrode kinetics in lithium battery electrodes: study in directionally freeze-cast LiNi 0.8 Co 0.15 Al 0.05 O 2 (NCA), J. Electrochem. Soc. 165 (2018) A388–A395 https://doi.org/, doi:10.1149/2.1321802jes.

[15] S. Levasseur, M. Ménétrier, E. Suard, C. Delmas, Evidence for structural defects in non-stoichiometric HT-$LiCoO_2$: electrochemical, electronic properties and 7Li NMR studies, Solid State Ionics 128 (2000) 11–24 https://doi.org/, doi:10.1016/S0167-2738(99)00335-5.

[16] I. Saadoune, C. Delmas, The insulator – metal transition upon lithium deintercalation from, J. Mater. Chem. 9 (1999) 1135–1140.

[17] L. Leyssens, B. Vinck, C. Van Der Straeten, F. Wuyts, L. Maes, Cobalt toxicity in humans—A review of the potential sources and systemic health effects, Toxicology 387 (2017) 43–56 https://doi.org/, doi:10.1016/j.tox.2017.05.015.

[18] S. Ahmed, P.A. Nelson, K.G. Gallagher, N. Susarla, D.W. Dees, Cost and energy demand of producing nickel manganese cobalt cathode material for lithium ion batteries, J. Power Sources. 342 (2017) 733–740 https://doi.org/, doi:10.1016/j.jpowsour.2016.12.069.

[19] S. Patoux, L. Sannier, H. Lignier, Y. Reynier, C. Bourbon, S. Jouanneau, F.Le Cras, S. Martinet, High voltage nickel manganese spinel oxides for Li-ion batteries, Electrochim. Acta. 53 (2008) 4137–4145 https://doi.org/, doi:10.1016/j.electacta.2007.12.054.

[20] P. Li, S. hua Luo, X. Wang, L. Wang, J. Wang, F. Teng, Q. Wang, Y. Zhang, X. Liu, H. Zhang, J. Liang, X. Duan, Study on the high-efficiency separation of Fe and Mn from low-grade pyrolusite and the preparation of $LiMn_2O_4$ materials for lithium-ion batteries, Sep. Purif. Technol. 278 (2022) 119611 https://doi.org/, doi:10.1016/j.seppur.2021.119611.

[21] J. Feng, B. Song, M.O. Lai, L. Lu, X. Zeng, Z. Huang, Electrochemical property of $LiMn_2O_4$ in over-discharged conditions, Funct. Mater. Lett. 5 (2012) 2–5 https://doi.org/, doi:10.1142/S1793604712500282.

[22] M. Park, X. Zhang, M. Chung, G.B. Less, A.M. Sastry, A review of conduction phenomena in Li-ion batteries, J. Power Sources. 195 (2010) 7904–7929 https://doi.org/, doi:10.1016/j.jpowsour.2010.06.060.

[23] J. Molenda, J. Marzec, K. Świerczek, W. Ojczyk, M. Ziemnicki, M. Molenda, M. Drozdek, R. Dziembaj, The effect of 3D substitutions in the manganese sublattice on the charge transport mechanism and electrochemical properties of manganese spinel, Solid State Ionics 171 (2004) 215–227 https://doi.org/, doi:10.1016/j.ssi.2004.04.022.

[24] J. Molenda, J. Marzec, K. Świerczek, D. Pałubiak, W. Ojczyk, M. Ziemnicki, The effect of 3D substitutions in the manganese sublattice on the electrical and electrochemical properties of manganese spinel, Solid State Ionics 175 (2004) 297–304 https://doi.org/, doi:10.1016/j.ssi.2004.01.069.

[25] S. Yamamura, H. Koshika, M. Nishizawa, T. Matsue, I. Uchida, In situ conductivity measurements of $LiMn_2O_4$ thin films during lithium insertion/extraction by using interdigitated microarray electrodes, J. Solid State Electrochem. 2 (1998) 211–215 https://doi.org/, doi:10.1007/s100080050090.

[26] S. Luo, D. Hu, H. Liu, J. Li, T.-.F. Yi, Hydrothermal synthesis and characterization of α-Fe_2O_3/C using acid-pickled iron oxide red for Li-ion batteries, J. Hazard. Mater. 368 (2019) 714–721 https://doi.org/, doi:10.1016/j.jhazmat.2019.01.106.

[27] S. zhi Yu, S. hua Luo, Y. Zhan, H. bo Huang, Q. Wang, Y. hui Zhang, Y. guo Liu, A. in Hao, Metal-organic framework-derived cobalt nanoparticle space confined in nitrogen-doped carbon polyhedra networks as high-performance bifunctional electrocatalyst for rechargeable Li–O_2 batteries, J. Power Sources. 453 (2020) 227899 https://doi.org/, doi:10.1016/j.jpowsour.2020.227899.

[28] S. xue Yan, Q. Wang, S. hua Luo, Y. hui Zhang, X. Liu, Y. guo Liu, Z. yuan Wang, A. min Hao, T. feng Yi, Coal-based S hybrid self-doped porous carbon for high-performance supercapacitors and potassium-ion batteries, J. Power Sources. 461 (2020) 228151 https://doi.org/, doi:10.1016/j.jpowsour.2020.228151.

[29] C. Liu, S. Luo, H. Huang, Y. Zhai, Z. Wang, Direct growth of MoO_2 /reduced graphene oxide hollow sphere composites as advanced anode materials for potassium-ion batteries, ChemSusChem 12 (2019) 873–880 https://doi.org/, doi:10.1002/cssc.201802494.

[30] C. Wei, H. Fei, Y. An, Y. Zhang, J. Feng, Crumpled Ti 3 C 2 T x (MXene) nanosheet encapsulated LiMn 2 O 4 for high performance lithium-ion batteries, Electrochim. Acta. 309 (2019) 362–370 https://doi.org/. doi:10.1016/j.electacta.2019.04.094.

[31] Y. Ein-Eli, S.H. Lu, M.A. Rzeznik, S. Mukerjee, X.Q. Yang, J. McBreen, LiCu x Mn2 − x O 4 Spinels (0.1 ⩽ x ⩽ 0.5) : a New Class of Cathode Materials for Li Batteries: II. In Situ Measurements, J. Electrochem. Soc. 145 (1998) 3383–3386 https://doi.org/. doi:10.1149/1.1838816.

[32] Y. Ein-Eli, J.T. Vaughey, M.M. Thackeray, S. Mukerjee, X.Q. Yang, J. McBreen, LiNi x Cu0.5 − x Mn1.5 O 4 spinel electrodes, superior high-potential cathode materials for Li Batteries: I. Electrochemical and structural studies, J. Electrochem. Soc 146 (1999) 908–913 https://doi.org/. doi:10.1149/1.1391699.

[33] Y.J. Wei, L.Y. Yan, C.Z. Wang, X.G. Xu, F. Wu, G. Chen, Effects of Ni doping on [MnO6] octahedron in LiMn 2O4, J. Phys. Chem. B. 108 (2004) 18547–18551 https://doi.org/. doi:10.1021/jp0479522.

[34] H. Zhao, X. Liu, C. Cheng, Q. Li, Z. Zhang, Y. Wu, B. Chen, W. Xiong, Synthesis and electrochemical characterizations of spinel LiMn1.94M04 (M = Mn0.06, Mg0.06, Si0.06, (Mg0.03Si0.03)) compounds as cathode materials for lithium-ion batteries, J. Power Sources. 282 (2015) 118–128 https://doi.org/. doi:10.1016/j.jpowsour.2015.02.049.

[35] C. Julien, S. Ziolkiewicz, M. Lemal, M. Massot, Synthesis, structure and electrochemistry of LiMn2-yAlyO4 prepared by a wet-chemistry method, J. Mater. Chem. 11 (2001) 1837–1842 https://doi.org/. doi:10.1039/b100030f.

[36] D. Capsoni, M. Bini, G. Chiodelli, P. Mustarelli, V. Massarotti, C.B. Azzoni, M.C. Mozzati, L. Linati, Inhibition of Jahn-Teller cooperative distortion in LiMn2O4 spinel by Ga3+ doping, J. Phys. Chem. B. 106 (2002) 7432–7438 https://doi.org/. doi:10.1021/jp020220u.

[37] M.M. Thackeray, C.S. Johnson, A.J. Kahaian, K.D. Kepler, J.T. Vaughey, Y. Shao-Horn, S.A. Hackney, Stabilization of insertion electrodes for lithium batteries, J. Power Sources. 81–82 (1999) 60–66 https://doi.org/. doi:10.1016/S0378-7753(98)00203-1.

[38] Y. Ein-Eli, LiNi[*sub* x]Cu[*sub* 0.5−*x*]Mn[*sub* 1.5]O[sub 4] spinel electrodes, superior high-potential cathode materials for Li batteries: I. Electrochemical and structural studies, J. Electrochem. Soc. 146 (1999) 908 https://doi.org/. doi:10.1149/1.1391699.

[39] Y. Ein-eli, W.F. Howard, Electrochemical society letters LiCu Cu ', -, Mn [2v (x + y) 04 5 V cathode materials, Elctrochemical Soc. Lett. 144 (1997) 205–207.

[40] A. Kraytsberg, Y. Ein-Eli, A. Kraytsberg, Y. Ein-Eli, Higher, stronger, better ... A review of 5 V cathode materials for advanced lithium-ion batteries, Adv. Energy Mater. 2 (2012) 922–939 https://doi.org/. doi:10.1002/aenm.201200068.

[41] D. Guo, B. Li, Z. Chang, H. Tang, X. Xu, K. Chang, E. Shangguan, X.Z. Yuan, H. Wang, Facile synthesis of LiAl0.1Mn1.9O4 as cathode material for lithium ion batteries: towards rate and cycling capabilities at an elevated temperature, Electrochim. Acta. 134 (2014) 338–346 https://doi.org/. doi:10.1016/j.electacta.2014.04.117.

[42] K.Y. Chung, W.S. Yoon, H.S. Lee, X.Q. Yang, J. McBreen, B.H. Deng, X.Q. Wang, M. Yoshio, R. Wang, J. Gui, M. Okada, Comparative studies between oxygen-deficient LiMn2O4 and Al-doped LiMn2O4, J. Power Sources. 146 (2005) 226–231 https://doi.org/. doi:10.1016/j.jpowsour.2005.03.033.

[43] D. Capsoni, M. Bini, G. Chiodelli, V. Massarotti, P. Mustarelli, L. Linati, M.C. Mozzati, C.B. Azzoni, Jahn-Teller transition in Al3+ doped LiMn2O4 spinel, Solid State Commun 126 (2003) 169–174 https://doi.org/. doi:10.1016/S0038-1098(03)00129-7.

[44] H. Dong, G.M. Koenig, Compositional control of precipitate precursors for lithium-ion battery active materials: role of solution equilibrium and precipitation rate, J. Mater. Chem. A. 5 (2017) 13785–13798 https://doi.org/. doi:10.1039/c7ta03653a.

[45] C. Cai, H. Dong, G.M. Koenig, Anisotropic particle synthesis and characterization for lithium-ion battery electrode materials via precursor precipitate growth inhibitor, Powder Technol 394 (2021) 214–224 https://doi.org/. doi:10.1016/j.powtec.2021.08.060.

[46] J. Rodríguez-Carvajal, Recent advances in magnetic structure determination by neutron powder diffraction, Phys. B Condens. Matter. 192 (1993) 55–69 https://doi.org/https://doi.org/. doi:10.1016/0921-4526(93)90108-I.

[47] T. Rosinel, J. Rodríguez-Carvajal, WinPLOTR: a Windows tool for powder diffraction patterns analysis T., (n.d.) 1–6.

[48] J.P. Robinson, G.M. Koenig, Tuning solution chemistry for morphology control of lithium-ion battery precursor particles, Powder Technol 284 (2015) 225–230 https://doi.org/. doi:10.1016/j.powtec.2015.06.070.

[49] D. Wang, I. Belharouak, G. Zhou, K. Amine, Synthesis of lithium and manganese-rich cathode materials via an oxalate co-precipitation method, J. Electrochem. Soc. 160 (2013) A3108–A3112 https://doi.org/. doi:10.1149/2.016305jes.

[50] K.S. Yoo, N.W. Cho, Y.-J. Oh, Structural and electrical characterization of Li(Mn1−δTiδ)2O4 electrode materials, Solid State Ionics 113–115 (1998) 43–49 https://doi.org/. doi:10.1016/S0167-2738(98)00365-8.

[51] T.T. Fang, H.Y. Chung, Reassessment of the electronic-conduction behavior above the verwey-like transition of Ni2+- and Al3+-doped LiMn2O 4, J. Am. Ceram. Soc. 91 (2008) 342–345 https://doi.org/. doi:10.1111/j.1551-2916.2007.02148.x.

[52] A. Iqbal, A.M. Khan, T. Wang, D. Li, Y. Gao, Effect of Ni and Cu substitution on the crystal structure, morphology and electrochemical performance of spinel LiMn2O4, Int. J. Electrochem. Sci. 14 (2019) 929–942 https://doi.org/. doi:10.20964/2019.01.79.

[53] C.D. ARUXANDEI, N. CORNEI, C.A. HUbANU, C.E. CIOMAGA, P.M. SAMOILA, A.R. IORDAN, M.N. PALAMARU, Sol-gel Synthesis and Characterization of LiMn, (n.d.).

[54] J. Liu, G. Li, Y. Yu, H. Bai, M. Shao, J. Guo, C. Su, X. Liu, W. Bai, Synthesis and electrochemical performance evaluations of polyhedra spinel LiAlxMn2-xO4 (x≦0.20) cathode materials prepared by a solution combustion technique, J. Alloys Compd. 728 (2017) 1315–1328 https://doi.org/. doi:10.1016/j.jallcom.2017.09.098.

[55] Q.C. Zhuang, T. Wei, L.L. Du, Y.L. Cui, L. Fang, S.G. Sun, An electrochemical impedance spectroscopic study of the electronic and ionic transport properties of spinel LiMn2O4, J. Phys. Chem. C. 114 (2010) 8614–8621 https://doi.org/. doi:10.1021/jp9109157.

[56] S. Ziolkiewicz, A. Rougier, G.A. Nazri, C.M. Julien, Electrical conductivity of LixMn2O4 with 0.60≤x≤1.18, Electrochem. Soc. Proc. 97 (1998) 145–151.

[57] M. Nishizawa, T. Ise, H. Koshika, T. Itoh, I. Uchida, Electrochemical in-situ conductivity measurements for thin film of Li(1-x)Mn2O4 spinel, Chem. Mater. 12 (2000) 1367–1371 https://doi.org/. doi:10.1021/cm990696z.

[58] T.F. Yi, Y.R. Zhu, R.S. Zhu, L. Zhou, P. Li, J. Shu, Physicochemical properties of LiAl x Mn 2ϵ-ϵx O4 and LiAl0.05Mn 1.95O4ϵ-ϵy F y cathode material by the citric acid-assisted sol-gel method, Ionics (Kiel) 15 (2009) 177–182 https://doi.org/. doi:10.1007/s11581-008-0248-6.

[59] G. Pistoia, D. Zane, Y. Zhang, Some aspects of LiMn2 O 4 electrochemistry in the 4 volt range, J. Electrochem. Soc. 142 (1995) 2551–2557 https://doi.org/. doi:10.1149/1.2050052.

[60] Y. Liu, T. Fujiwara, H. Yukawa, M. Morinaga, Lithium intercalation and alloying effects on electronic structures of spinel lithium manganese oxides, Sol. Energy Mater. Sol. Cells. 62 (2000) 81–87 https://doi.org/. doi:10.1016/S0927-0248(99)00138-5.

[61] C.Y. Ouyang, S.Q. Shi, M.S. Lei, Jahn-Teller distortion and electronic structure of LiMn2O4, J. Alloys Compd. 474 (2009) 370–374 https://doi.org/. doi:10.1016/j.jallcom.2008.06.123.

[62] S. Mandal, R.M. Rojas, J.M. Amarilla, P. Calle, N.V. Kosova, V.F. Anufrienko, J.M. Rojo, High temperature Co-doped LiMn 2 O 4 -based spinels, Structural, Electrical, and Electrochemical Characterization (2002) 1598–1605.

[63] A.H. Marincaş, F. Goga, S.A. Dorneanu, P. Ilea, Review on synthesis methods to obtain LiMn2O4-based cathode materials for Li-ion batteries, J. Solid State Electrochem. 24 (2020) 473–497 https://doi.org/. doi:10.1007/s10008-019-04467-3.

[64] T. Ohzuku, M. Kitagawa, T. Hirai, Electrochemistry of manganese dioxide in lithium nonaqueous cell: III . X-ray diffractional study on the reduction of electrolytic manganese dioxide, J. Electrochem. Soc. 136 (1989) 3169–3174 https://doi.org/. doi:10.1149/1.2096421.

[65] Z. Cai, Y. Ma, X. Huang, X. Yan, Z. Yu, S. Zhang, G. Song, Y. Xu, C. Wen, W. Yang, High electrochemical stability Al-doped spinel LiMn2O4 cathode material for Li-ion batteries, J. Energy Storage. 27 (2020) https://doi.org/. doi:10.1016/j.est.2019.101036.

[66] I. Belharouak, G.M. Koenig, T. Tan, H. Yumoto, N. Ota, K. Amine, Performance Degradation and Gassing of Li 4 Ti 5 O 12 /LiMn 2 O, J. Electrochem. Soc. 159 (2012) A1165–A1170 https://doi.org/. doi:10.1149/2.013208jes.

[67] K. Amine, J. Liu, S. Kang, I. Belharouak, Y. Hyung, D. Vissers, G. Henriksen, Improved lithium manganese oxide spinel/graphite Li-ion cells for high-power applications, J. Power Sources. 129 (2004) 14–19 https://doi.org/. doi:10.1016/j.jpowsour.2003.11.007.

[68] Y. Ein-Eli, S.H. Lu, M.A. Rzeznik, S. Mukerjee, X.Q. Yang, J. McBreen, LiCu x Mn2 − x O 4 Spinels (0.1 ⩽ x ⩽ 0.5) : a new class of cathode materials for Li batteries: II. In situ measurements, J. Electrochem. Soc. 145 (1998) 3383–3386 https://doi.org/. doi:10.1149/1.1838816.

[69] Y. Ein-Eli, W.F. Howard, S.H. Lu, S. Mukerjee, J. McBreen, J.T. Vaughey, M.M. Thackeray, LiMn2 − x Cu x O4 Spinels (0.1 ⩽ x ⩽ 0.5): a new Class of 5 V Cathode materials for Li batteries: I. Electrochemical, structural, and spectroscopic studies, J. Electrochem. Soc. 145 (1998) 1238–1244 https://doi.org/. doi:10.1149/1.1838445.

[70] S. Mukerjee, X.Q. Yang, X. Sun, S.J. Lee, J. McBreen, Y. Ein-Eli, In situ synchrotron X-ray studies on copper-nickel 5 V Mn oxide spinel cathodes for Li-ion batteries, Electrochim. Acta. 49 (2004) 3373–3382 https://doi.org/. doi:10.1016/j.electacta.2004.03.006.

[71] M. Yang, B. Xu, J. Cheng, C. Pan, B. Hwang, Y.S. Meng, Electronic, structural, and electrochemical properties spinel materials, Chem. Mater. 23 (2011) 2832–2841.

[72] A. Yamada, M. Tanaka, Jahn-Teller structural phase transition around 280 K in LiMn2O4, Mater. Res. Bull. 30 (1995) 715–721 https://doi.org/. doi:10.1016/0025-5408(95)00048-8.

[73] Y.K. Lee, J. Park, W. Lu, Electronic and bonding properties of LiMn 2 O 4 spinel with different surface orientations and doping elements and their effects on manganese dissolution, J. Electrochem. Soc. 163 (2016) A1359–A1368 https://doi.org/. doi:10.1149/2.0991607jes.

[74] Ł. Kondracki, J. Molenda, Beneficial effect of phase transition on kinetics of deintercalation/intercalation process in lithium–manganese spinel, J. Solid State Electrochem. 23 (2019) 837–846 https://doi.org/. doi:10.1007/s10008-018-04187-0.

[75] J. Molenda, W. Ojczyk, M. Marzec, J. Marzec, J. Przewoźnik, R. Dziembaj, M. Molenda, Electrochemical and chemical deintercalation of LiMn2O4, Solid State Ionics 157 (2003) 73–79 https://doi.org/. doi:10.1016/S0167-2738(02)00191-1.

[76] J.B. Goodenough, A. Manthiram, B. Wnetrzewski, Electrodes for lithium batteries, J. Power Sources. 43 (1993) 269–275 https://doi.org/. doi:10.1016/0378-7753(93)80124-8.

[77] A. Van Der Ven, C. Marianetti, D. Morgan, G. Ceder, Phase transformations and volume changes in spinel LixMn2O4, Solid State Ionics 135 (2000) 21–32 https://doi.org/, doi:10.1016/S0167-2738(00)00326-X.
[78] K.Y. Chung, K.B. Kim, Investigations into capacity fading as a result of a Jahn-Teller distortion in 4 V LiMn2O4 thin film electrodes, Electrochim. Acta. 49 (2004) 3327–3337 https://doi.org/, doi:10.1016/j.electacta.2004.01.071.
[79] Y. Shao-Horn, S.A. Hackney, A.J. Kahaian, K.D. Kepler, E. Skinner, J.T. Vaughey, M.M. Thackeray, Structural fatigue in spinel electrodes in Li/Lix[Mn2]O4 cells, J. Power Sources. 81–82 (1999) 496–499 https://doi.org/, doi:10.1016/S0378-7753(98)00223-7.
[80] M.M. Thackeray, Y. Shao-Horn, A.J. Kahaian, K.D. Kepler, E. Skinner, J.T. Vaughey, S.A. Hackney, Structural fatigue in spinel electrodes in high voltage (4V) Li/LixMn2O4 cells, Electrochem. Solid-State Lett. 1 (1998) 7–9 https://doi.org/, doi:10.1149/1.1390617.
[81] A. Fly, R. Chen, Rate dependency of incremental capacity analysis (dQ/dV) as a diagnostic tool for lithium-ion batteries, J. Energy Storage. 29 (2020) 101329 https://doi.org/, doi:10.1016/j.est.2020.101329.
[82] B. Zhao, R. Ran, M. Liu, Z. Shao, A comprehensive review of Li 4 Ti 5 O 12 -based electrodes for lithium-ion batteries : The latest advancements and future perspectives, 98 (2015) 1–71.
[83] D. Young, A. Ransil, R. Amin, Z. Li, Y.M. Chiang, Electronic conductivity in the Li4/3Ti5/3O 4-Li7/3Ti5/3O4 system and variation with state-of-charge as a Li battery anode, Adv. Energy Mater. 3 (2013) 1125–1129 https://doi.org/, doi:10.1002/aenm.201300134.
[84] Z. Nie, R. Parai, C. Cai, C. Michaelis, J.M. LaManna, D.S. Hussey, D.L. Jacobson, D. Ghosh, G.M. Koenig, Pore microstructure impacts on lithium ion transport and rate capability of thick sintered electrodes, J. Electrochem. Soc. 168 (2021) 060550 https://doi.org/, doi:10.1149/1945-7111/ac0bf6.
[85] K. Ragavendran, H. Xia, P. Mandal, A.K. Arof, Jahn-Teller effect in LiMn2O4: influence on charge ordering, magnetoresistance and battery performance, Phys. Chem. Chem. Phys. 19 (2017) 2073–2077 https://doi.org/, doi:10.1039/c6cp07289e.
[86] Y. Shimakawa, T. Numata, J. Tabuchi, Verwey-type transition and magnetic properties of the LiMn2O4Spinels, J. Solid State Chem. 131 (1997) 138–143 https://doi.org/, doi:10.1006/jssc.1997.7366.
[87] D. Capsoni, M. Bini, G. Chiodelli, V. Massarotti, C.B. Azzoni, M.C. Mozzati, A. Comin, Inhibition of Jahn Teller cooperative distortion in LiMn2O4 spinel by transition metal ion doping, Phys. Chem. Chem. Phys. 3 (2001) 2162–2166 https://doi.org/, doi:10.1039/b100080m.
[88] X. Tang, J. Zhou, M. Bai, W. Wu, S. Li, Y. Ma, Investigation of the self-discharge behaviors of the LiMn2O4 cathode at elevated temperatures:: In situ X-ray diffraction analysis and a co-doping mitigation strategy, J. Mater. Chem. A. 7 (2019) 13364–13371 https://doi.org/, doi:10.1039/c9ta02718a.
[89] B. Ebin, M. Doeff, V. Battaglia, Effects of the particle properties on electrochemical performance of nanocrystalline LiAl0.1Cu0.1Mn1.8O4 cathode materials prepared by ultrasonic spray pyrolysis, J. Electroanal. Chem. 792 (2017) 1–7 https://doi.org/, doi:10.1016/j.jelechem.2017.03.031.